

Effect of wear particles and roughness on nanoscale friction

Tobias Brink,^{*} Enrico Milanese,[†] and Jean-François Molinari

*Civil Engineering Institute and Institute of Materials Science and Engineering,
École polytechnique fédérale de Lausanne (EPFL), Station 18, CH-1015 Lausanne, Switzerland*

(Dated: January 19, 2022)

Frictional contacts lead to the formation of a surface layer called the third body, consisting of wear particles and structures resulting from their agglomerates. Its behavior and properties at the nanoscale control the macroscopic tribological performance. It is known that wear particles and surface topography evolve with time and mutually influence one another. However, the formation of the mature third body is largely uncharted territory and the properties of its early stages are unknown. Here we show how a third body initially consisting of particles acting as roller bearings transitions into a shear-band-like state by forming adhesive bridges between the particles. Using large-scale atomistic simulations on a brittle model material, we find that this transition is controlled by the growth and increasing disorganization of the particles with increasing sliding distance. Sliding resistance and wear rate are at first controlled by the surface roughness, but upon agglomeration wear stagnates and friction becomes solely dependent on the real contact area in accordance with the plasticity theory of contact by Bowden and Tabor.

I. INTRODUCTION

When surfaces come into frictional contact, they can undergo structural, morphological, and/or chemical changes. A surface layer forms, the so-called third body (or “gouge” in geophysics), which consists of wear particles detached during sliding, consolidated debris, and an altered sub-surface layer [1]. While this is often a nanometer or micrometer-sized object, it impacts and controls friction and wear at the macroscopic scale [1–5]. A significant difficulty in the study of the third body is that it forms at an interface that is generally inaccessible *in situ* [6, 7]. Experiments are thus only amenable to post-mortem analysis without a detailed understanding of the dynamics and mechanisms. Even the simplest case of adhesive wear of unlubricated surfaces, which we are concerned with in the present work, is due to a complex interplay of different mechanisms. We nevertheless know, partially thanks to computer simulations that allow *in silico* investigation on the atomistic length scale, that wear particles appear and evolve in tandem with the surface roughness in inseparably entangled processes [6, 8–11]. In a typical two-body contact, third body formation commences by the detachment of wear particles based on the morphology of the contacts between the surfaces [1, 3–5, 12–15]. These particles work the surface and interact with each other, possibly agglomerating [1, 3, 10, 11, 16]. Many atomistic simulations addressing third-body rheology have been reported in the literature, but they have either not been able to capture wear particle formation [17–21], neglected surface roughness [22–25], used two-dimensional models

[10, 11, 15], restricted the movement of wear particles [26], or used only a single wear particle [10, 11, 15]. Here, we present molecular dynamics (MD) computer simulations with a multi-particle, three-dimensional setup with fully plastically-deformable, rough surfaces.

II. METHODS

All simulations in the present work were molecular dynamics simulations performed using the software LAMMPS [27] with GPU-accelerated potentials [28, 29].

A. Model material

The formation of wear particles has a size dependence that is a function of material properties, where asperity-asperity contacts below a critical size d^* cannot lead to the detachment of particles [12]. The relevant length scales for wear are smaller for hard and brittle materials. Therefore we chose to use a silicon-like model material, which has been modified to be more brittle than real silicon [14, 30, 31] in order to be able to observe wear particle interactions under sustained rolling conditions. The material was nanocrystalline with average grain sizes of 3 nm to make it more isotropic and to accelerate the wear process (see Appendix A for tests and comparisons with other material choices).

The material used for the main part of our work has a diamond crystal structure with a lattice constant of 0.543 nm. Using a pure shear simulation of the bulk material with an engineering shear rate of 10^8 s^{-1} , we found a shear strength of $\tau = 6.6 \text{ GPa}$ and estimated the hardness as $H \approx 3\sqrt{3}\tau = 34.5 \text{ GPa}$. The material has a Young’s modulus of 149.5 GPa, a Poisson ratio of 0.23, and a shear modulus of $G = 60.6 \text{ GPa}$. The single crystal has a $\{111\}$ surface energy of $\gamma = 1.6 \text{ J/m}^2$, which we take to be approximately half the fracture energy due to the

^{*} t.brink@mpie.de; Present address: Max-Planck-Institut für Eisenforschung GmbH, Max-Planck-Straße 1, 40237 Düsseldorf, Germany

[†] Present address: Department of Earth, Atmospheric, and Planetary Sciences, Massachusetts Institute of Technology, Cambridge, MA, USA

brittleness of the material. Wear particles are expected to form at asperities with sizes exceeding a diameter of [12] $d^* \approx 12\gamma G\tau^{-2} = 27$ nm. Asperities and contacts with a diameter below d^* will not detach during sliding, but only deform plastically [12]. The value of d^* for a fully amorphous system would be roughly half of that [14] and we thus expect the value for the nanocrystal to lie in between those two values, since the grain boundaries are expected to have lower fracture resistance.

B. Simulation setup

To prepare the sliding simulations, two first bodies consisting of the bulk material were prepared with periodic boundary conditions in x and y direction. In z direction, we used pre-worn surfaces to speed up the running-in process (see Appendix B). The initial third body consists of several, independent rigid particles with the same interatomic potential as the bulk material. We chose not to model the particle formation process for considerations of computational efficiency, since it has been investigated before in detail [10–16]. For the main simulations, we used 16 particles in the shape of rhombicuboctahedra with a diameter of about 8 nm arranged on a regular grid, which is roughly on the order of the minimal particle diameter d^* at its formation (see Appendix B for different choices of initial particle shape and placement).

The two first bodies each had a size of $58 \times 58 \times 11$ nm³ (around 3,200,000 atoms for the whole simulation), where the topmost and lowermost layers of width 0.4 nm in z direction were treated as rigid boundaries to apply normal force and sliding displacement. Possible size effects are discussed in Appendix B. The energy of the system was minimized to avoid large forces due to any closely-spaced atoms that might have appeared during the preparation. The systems were then equilibrated with a Nosé–Hoover thermostat at 300 K and barostats at ambient pressure in x and y direction. The target normal force F_N was applied on the boundaries in z direction. This equilibration was performed for 1 ns with a time integration step of 1 fs.

After equilibration, sliding simulations with a velocity of 20 m/s were performed over a given sliding distance s . The sliding direction was chosen to be 8.5° off the x direction to avoid wear particles moving along the same groove during the whole simulation due to the periodic boundary conditions. The sliding velocity was initially applied to the whole upper body and continuously enforced at the top boundary throughout the simulation. The lower boundary was kept fixed. The reaction forces in sliding direction at the boundaries then equal the friction force F_T . To keep the simulations isothermal at room temperature, Langevin thermostats with a damping constant of 0.01 ps were applied in the regions next to the top and bottom boundaries over a width of 0.4 nm. The center-of-mass velocity of the top thermostat region was subtracted before applying the thermostat in order to avoid an artificial drag force.

We also performed some verification simulations to investigate the influence of sliding velocity and the choice of rigid particles instead of plastically deformable ones. This is described in Appendix C.

C. Surface reconstruction and characterization

In order to be able to cleanly delineate the surface from the third body, the wear particles must be separated from the first bodies. For this, we simply fixed the rigid wear particles in space and applied a velocity of 20 m/s in z direction to each boundary to pull the bodies apart. In some cases with larger wear volume, wear fragments not belonging to the rigid particles stuck to one of the surfaces, in which case we also fixed a region of width 1 nm in the center of the tribolayer. At the end of the separation process, the atomic positions were minimized with regard to the potential energy to remove the frozen thermal vibrations for the analysis.

Since atoms in MD simulations are modeled as mass points, the notion of a surface is ill defined without further specifications. Here, we used a surface mesh generation algorithm [32] as implemented in OVITO [33] to find atoms that belong to a surface of the volume that is impenetrable to a virtual probe sphere. We chose the radius of the probe sphere to roughly correspond to the average second-neighbor distance of 3.85 Å for silicon.

As a simple parameter for describing the surface roughness, we used the rms of heights $h_{\text{TMS}} = \langle (z_i - \langle z_i \rangle)^2 \rangle^{1/2}$, where z_i is the z component of the position of the surface atoms and $\langle \dots \rangle$ is the arithmetic mean. Both first bodies were made of the same material, so they quickly attained the same value of h_{TMS} , even during the running-in phase. We therefore use the arithmetic mean of the values for both surfaces from here on.

D. Estimation of wear volume and third body thickness

The wear volume V was estimated from the separated third body in the middle of the simulation box. For this, we calculated the average atomic volume in the tribolayer by Voronoi tessellation [34] as $\Omega = 21.292 \times 10^{-3}$ nm³. The wear volume is thus defined as the number of atoms in the third body (excluding the initially inserted wear particles) times Ω .

We defined the distance g between the surfaces of the two first bodies—which we also define as the thickness of the third body and which is approximately equal to the diameter of the wear particles—with the help of a density profile along the z direction of the non-separated simulation boxes. Since the density in the tribolayer is lower, we defined the average surfaces of the first bodies by taking the half height between minimum and maximum density on both sides of the third body [inset of Fig. S1(a) in the Supplemental Material [35]]. We take the distance

between these two points as the thickness g of the third body. It is also possible to verify the wear volume by integrating over the density data in the tribolayer. This method mostly agrees with the first method described above [Fig. S1(b) in the Supplemental Material [35]].

E. Contact area

The real contact area A_c between the third body and the first bodies was computed by marking the atoms belonging to the third body (obtained via the separation method outlined above) and considering all atoms in the first bodies that are closer than 0.3 nm to the third body to be in contact. The cutoff was chosen as the first minimum in the pair distribution function. To convert the number of contacting atoms to an area, we used a typical surface, calculated its area and the number of surface atoms using surface mesh generation [32], and arrived at a surface area per surface atom of 0.1053 nm^2 .

III. RESULTS

A. The third body

The introduction of rigid wear particles between two bodies in relative sliding motion [Fig. 1(a)] first leads to a relatively short running-in phase, in which the surface morphology evolves quickly and the particles become coated with material picked up from both surfaces [Fig. 1(b) and video `run-in.webm` in the companion dataset [36]]. Due to this coating, the wear process resembles the adhesive wear case with comparable material properties in all three bodies [6], despite the artificial rigidity of the initial particles (see Appendix C for a detailed discussion of the difference between rigid and plastically deformable particles). The surfaces of the two first bodies become amorphous up to a depth of around 1 to 3 nm. In the common scenario of adhesive wear of initially bare surfaces, this phase would instead be dominated by the formation of wear particles [10, 12–14, 16], which we bypassed here.

As expected from two-dimensional modeling and theory [10, 11, 16], the spherical particles continue to grow. In three dimensions, though, the easiest growth direction is into the empty space lateral to the sliding direction, leading to the formation of cylindrical rollers illustrated in Fig. 1(b)–(d) and the video `rolling.webm` in the companion dataset [36]. Such cylindrical debris particles have been observed experimentally in brittle and quasi-brittle materials [37–46], and their appearance relates to a weakening of the interface (i.e. a drop in the friction coefficient) [40, 46]. In rock experiments [45], the interface strengthens upon further sliding and then weakens again. This evolution is attributed to the formation and full development of a layer where shear localizes. Yet the transition from powder rolling to shear localization is still unclear.

In our simulations of the brittle model material, the persistence of the regime of cylindrical rollers is contingent upon either a regular spacing of the cylindrical particles or large distances between them. Figure 1(e)–(f) shows that interactions between the particles lead to agglomeration and a breakdown of the rolling regime. A very porous, shear-band-like state emerges. If our simulations start with wear particles arranged on a regular grid, this shear-band-like state is delayed and sometimes does not occur within the time scale of the simulations. If the particles are initially placed randomly instead, interactions between them destabilize the rolling regime immediately

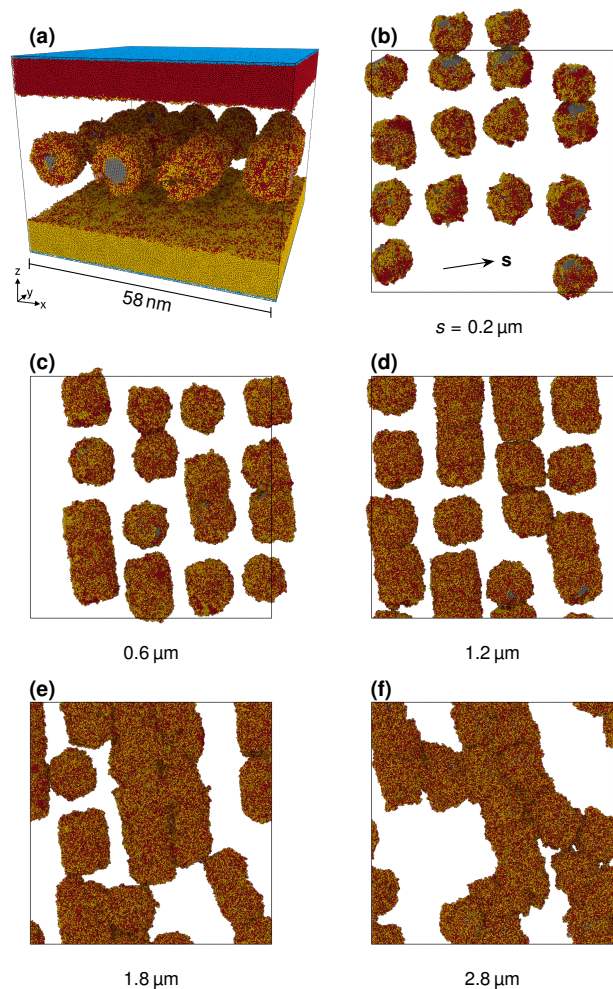


Figure 1. Early stages of the third body. (a) Particles were introduced between two surfaces and subjected to sliding motion. Panels (b)–(f) show only the third body as it evolves from spherical particles (b), to cylindrical rollers (c)–(d), to a porous, shear-band-like state (e)–(f). Atoms are colored according to the body they originally belonged to, namely top surface (red), bottom surface (yellow), third body (gray), or boundary (blue). The box indicates the periodic boundaries and atoms are shown outside if it makes the shape of the particle clearer. The sliding direction is indicated in panel (b).

(Fig. S2 in the Supplemental Material [35] and video `sb-like-regime.webm` in the companion dataset [36]).

We tried to reproduce this evolution also with realistic, metallic materials, such as Cu, Al, Ni, a high-entropy alloy, and a metallic glass, but the friction coefficient quickly reaches or exceeds a value of 1.0 (see Appendix A and Fig. S3 in the Supplemental Material [35]). These systems react by scratching due to the abrasive particles and quickly weld. This is on one hand due to their lower hardness and the lack of bond directionality, which lead to much higher adhesion and plasticity, thereby suppressing the rolling of wear particles more easily. On the other hand, the typical size of wear particles due to adhesive wear is expected to be much larger in metals than can be simulated using MD [12]. Nevertheless, we are not aware of any work that observes cylindrical particles acting as roller bearings in metals. The following sections thus focus on the brittle model material simulations.

B. Friction

In the framework of Bowden and Tabor [47], the frictional force F_T arises as a result of the shear strength τ of adhesive contacts between two bodies as $F_T = \tau A_c$. The real contact area A_c is smaller than the macroscopic, apparent contact area A and is proportional to the normal load F_N [Fig. 2(a)]. At small scales, part of the

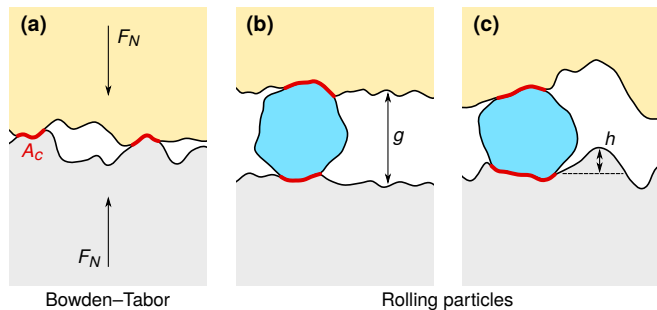


Figure 2. Influence of roughness on friction. (a) In Bowden and Tabor’s model, friction is due to the real contact area $A_c \propto F_N$. The proportionality is a consequence of the fractal nature of the surface roughness, where more asperities come into contact with increasing load. (b) When the system includes wear particles, this simple proportionality is insufficient to explain the friction force, which now also depends on the rolling friction of the particles. Nevertheless, there is still a contact area between the third-body particle and the two first bodies, which can lead to friction due to adhesive forces. (c) At least on the nanoscale, the roughness may be large compared to the particle size and therefore increase friction by presenting obstacles in the form of surface asperities to the smooth rolling motion of the particles. Configurations with large asperities should be unstable, since the obstacles are worn off (or the particle is reincorporated into the surface). The influence of roughness—i.e., the asperity heights h —has to be related to the particle size, here approximated by the thickness g of the third body.

real contact area is also due to adhesion. This results in the typical Amontons–Coulomb friction law [48], where $F_T = \mu F_N + F_{\text{adh}}$ with μ being the friction coefficient, a proportionality constant, and F_{adh} representing the adhesive contribution at zero normal load. Previous works found that this model is valid even at the nanoscale [22], but third bodies or significant surface roughness were not considered. Simulations of abrasive particles with fixed positions in space grinding a moving metal surface (resembling for example polishing with sandpaper) also recovered the Bowden–Tabor relation of friction to contact area at the nanoscale [26], but did not consider the evolution and movement of the particles. In contrast, later macroscopic model experiments with mobile, elastic third-body particles and surfaces, as well as low adhesion, highlight the importance of the ratio of surface roughness to wear particle size rather than contact area [9].

In our case, we can observe the effects of plastic deformation, wear, and strong adhesion that are expected to dominate the response at the nanoscale. Figure 3(a) shows that the friction force has no clear dependence on the contact area in the rolling regime. Indeed, the same friction force is observed for whole ranges of contact area for a given F_N . The linearity between A_c and F_T is recovered when entering the shear-band-like regime.

If the friction force for a given normal load is constant or even slightly negatively correlated with the contact area, another parameter must be modifying the response. It stands to reason that—given a constant real contact area—friction on a rougher surface should be higher. We expect this to be in relation to the size of the rolling particles (approximated by the third body thickness g). Here, we introduce a relative surface roughness, expressed in terms of the rms of heights h_{rms} divided by g , with the reasoning being that asperities with heights of the same order as the particle diameter represent obstacles, while much smaller asperities barely influence the rolling motion [Fig. 2(b)–(c)]. Figure 3(b) shows that this variable is a good predictor of the friction force in the rolling regime, leading to a friction law of the form

$$\frac{F_T}{F_N} = \mu_0^r + \mu_1^r \frac{h_{\text{rms}}}{g} \quad (1)$$

with fit parameters $\mu_0^r = 0.13$ and $\mu_1^r = 2.09$. The first term resembles Amontons–Coulomb friction. In Fig. 3(c) the frictional force minus the roughness-dependent term of Eq. 1 is plotted over the real contact area. There is now a proportionality between these quantities: $F_T - \mu_1^r F_N h_{\text{rms}}/g \approx f \tau A_c$ with $f = 0.1$. We can thus also write Eq. 1 as

$$F_T = f \tau A_c + \mu_1^r \frac{h_{\text{rms}}}{g} F_N, \quad (2)$$

obtaining a version of Bowden and Tabor’s friction model for the first term, although with a significantly reduced shear strength. The proportionality between F_N and A_c changes during wear of the surfaces, meaning that there

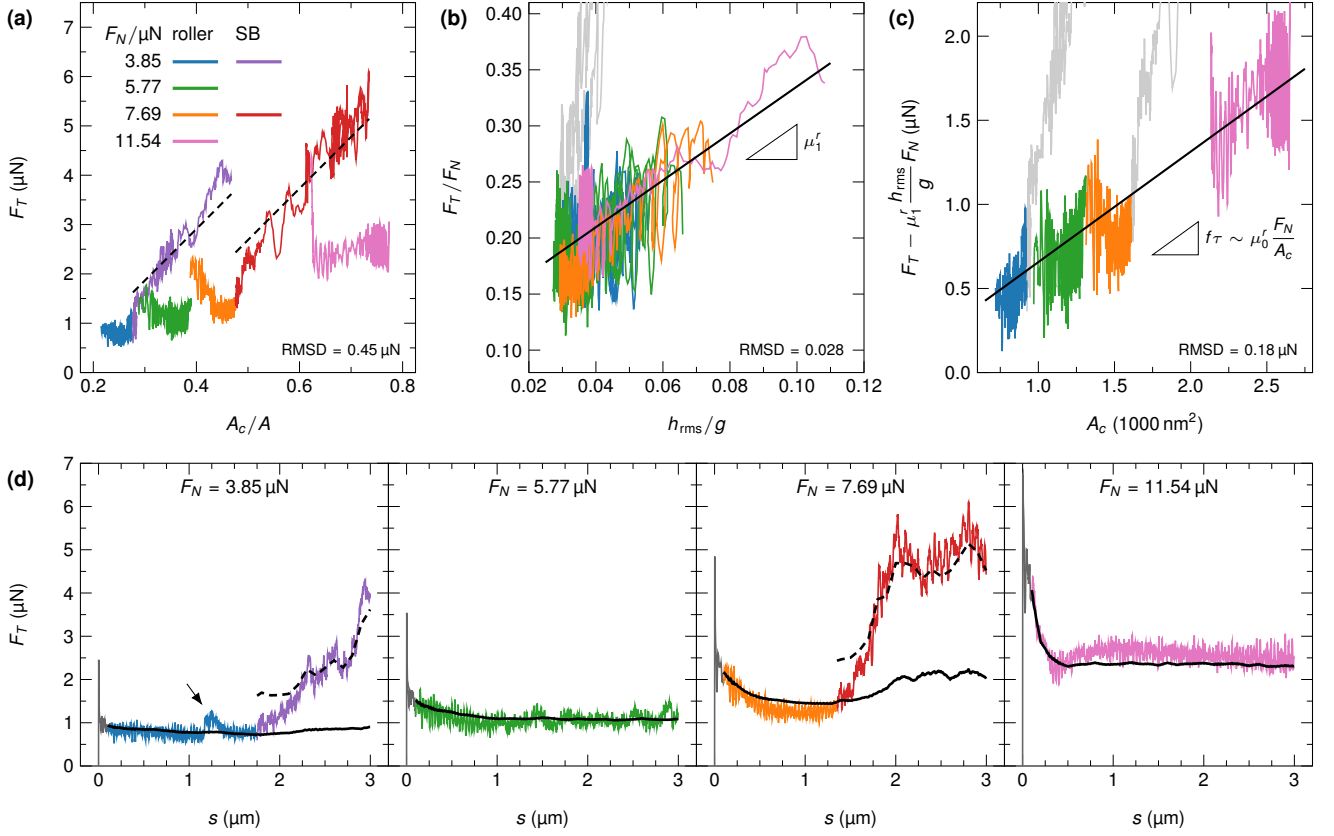


Figure 3. Friction force as a function of contact area, roughness, and sliding distance. (a) The friction force plotted over the relative contact area reveals that a direct linear dependence between the two quantities only exists in the shear-band-like regime (SB), while the friction force of the cylindrical rollers does not vary with the contact area for a given normal load, or even seems to be slightly negatively correlated. The dashed lines represent fits to the friction law in Eq. 3. (b) The friction of the rollers is instead correlated with the surface roughness divided by the third-body thickness, in accordance with Eq. 1 (solid black line). The light gray lines represent the data from the shear-band-like regime, for which the roughness data is much less reliable. (c) Subtracting the roughness-dependent term of Eq. 1 from the frictional force reveals a linear relation between the remaining partial friction force and the real contact area (solid black line). This explains the apparent, partially negative correlation between F_T and A_c : When the contact area increases after running-in, it is counteracted by the roughness decreasing at the same time. The slope is indirectly related to the friction coefficient μ_0^r of a flat surface. (a)–(c) The root-mean-square deviation (RMSD) is provided as a goodness-of-fit measure. (d) The friction laws in this work (Eqs. 1, solid lines and Eq. 3, dashed lines) fit well to the friction force data plotted over sliding distance. The arrow shows a point in time when two cylinders temporarily stick together, leading to the transient friction peak when the pure rolling motion is disturbed.

is no simple relation between $f\tau$ and μ_0^r . Our results show that the effective shear strength is expectedly lower for the rolling regime ($f\tau$ with $f < 1$) than for the sliding contact (τ) envisioned in the original model.

When transitioning to the shear-band-like third body, there is a direct dependence on contact area [Fig. 3(a) and Fig. S2 in the Supplemental Material [35]], but not all the area seems to participate:

$$F_T = \tau^{\text{SB}}(A_c - A_0) \quad (3)$$

with $\tau^{\text{SB}} = 3.1 \text{ GPa}$. The bulk shear strength of the amorphous material (as expected in the third body) is around 4.9 GPa [14], meaning that the third body has a lower shear strength than the bulk material, but a higher strength than the rolling interface ($f\tau \approx 0.7 \text{ GPa}$ in Eq. 2). The term depending on the relative roughness

disappears together with the rolling motion of the wear particles. The reduction of the participating contact area by A_0 compared to Bowden and Tabor’s model is on one hand due to parts of the third body still rolling and on the other hand due to some uncertainty in assigning a correct contact area per atom.

Taking both regimes into account, the friction force is well reproduced by Eqs. 1 and 3 over the whole sliding distance [Fig. 3(d)].

C. Wear

The wear behavior of the system is plotted in Fig. 4(a). Since no volume can be lost in the simulation setup due to periodic boundaries, we define the wear volume as the

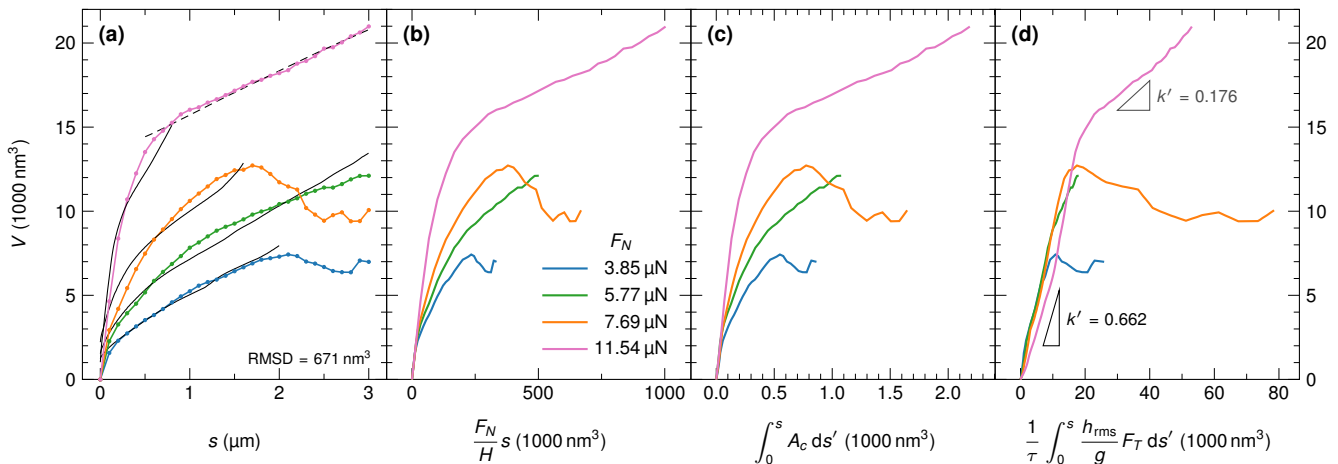


Figure 4. (a) Cumulative wear volume as a function of sliding distance for different normal loads. Parts of the wear volume data are linearly dependent on the sliding distance in the steady-state regime. The slopes, representing the wear rates, though, seem to be comparable for different normal loads. (b) By plotting the wear volume as a function of $F_N s/H$ as in Archard’s wear equation, the slopes should represent the wear coefficient k , which would be independent of F_N in Archard’s model. The data shows that this is not the case: the slopes are different and the data do not collapse onto a single curve. (c) In the original derivation of this equation, it is $F_N/H = A_c$. Therefore we also plot the wear volume as a function of the integral over a direct measurement of the contact area, but do not obtain a better correlation. (d) However, if we replace the normal load F_N by the tangential friction force F_T modified by a roughness term h_{rms}/g , we obtain the same linear relation for all curves including the running-in phase—although excluding the low-wear, shear-band-like regime—with a constant $k' = 0.662$ (see Eq. 6). Note that the cylinders in the simulation with $F_N = 11.54 \mu\text{N}$ start spanning across the periodic boundaries at $s = 0.5 \mu\text{m}$, forcing a rolling direction at an angle to the sliding direction. This adds a shear component which leads to bidirectional exchange of material between first and third bodies and reduces the efficiency of the wear process to $k' = 0.176$. The resulting best fits are also shown in (a) as black lines (solid line for $k' = 0.662$ and dashed line for $k' = 0.176$) together with the RMSD as a goodness-of-fit measure for the solid lines.

volume of the third body. After the running-in phase with a high wear rate, the rolling regime exhibits a roughly constant wear rate as it is typically also observed in macroscopic wear [49–51]. In the macroscopic case, the wear volume V is predicted by Archard’s semi-empirical wear equation [52, 53]

$$\frac{V_{\text{Archard}}}{s} = k \frac{F_N}{H}, \quad (4)$$

with sliding distance s , hardness H , and wear coefficient k . In the present work, the wear rate is comparable between the simulations with different normal load [slope of the curves in Fig. 4(a)], which means that this system does not follow Archard’s prediction. The data does not collapse onto a single curve when plotted as a function of $F_N s/H$, indicating a change of k with normal load [Fig. 4(b)]. In the original derivation, the equation can also be expressed as $V/s = k A_c$, with F_N/H being an approximation of the contact area. While this is able to account for changing contact areas during sliding, it does not differ qualitatively from the results using Eq. 4 [Fig. 4(c)]. A different approach is required.

In the case of wear particle formation with significant plastic activity, it has been found that the wear volume in the single-asperity case is related to the tangential work

by [13]

$$V_{\text{asp}} = \frac{\int_0^s F_T ds'}{\omega \tau} \quad (5)$$

with ω being a shape factor close to unity (see Fig. S4 in the Supplemental Material [35]). Here, all dissipated energy is used to detach the particle.

Rolling wear particles should constantly pick up volume and wear the surface by a fracture process [16]. In our case, the wear particles interact with asperities of the rough surface and we consequently found that a similar approach to the asperity–asperity interaction also applies to wear in the rolling regime:

$$V = \frac{k'}{\tau} \int_0^s \frac{h_{\text{rms}}}{g} F_T ds' \quad (6)$$

with $k' = 0.662$ independent of the applied normal load [Fig. 4(d)]. We included a measure of the relative roughness to achieve this, which plays a similar role to the classical wear coefficient: it describes the efficiency of the wear process. While in the asperity–asperity collision described by Eq. 5 almost all of the tangential work is expended to detach the wear particle, only part of the friction is due to wear particle formation and growth in more complex and realistic scenarios. We reason that the nanoscale wear events should be more likely if the

asperities present larger obstacles to the rolling particles, and thus that h_{rms}/g is a reasonable measure of the wear efficiency. This assumption allows us to also capture the running-in phase, which is characterized by a higher roughness. The remaining empirical parameter k' is close, but not equal, to unity, indicating that the physics of the present system can be described adequately with the proposed physical quantities in Eq. 6. The relative roughness h_{rms}/g lies in the range of 0.02–0.08 in the steady rolling regime, and therefore makes the wear much less efficient than in the case of wear particle formation.

In the shear-band-like regime, the wear volume stagnates. While there is a bias to pick up volume in the rolling regime [10, 16], matter exchanges in both directions between surface and the shear-band-like third body. Wear damage could still occur by growth of the shear band, although the width of the tribolayer stagnates at least on the timescale of our simulations (Fig. S1 in the Supplemental Material [35]). This is thus the least efficient wear mode, since wear rates are low or zero and friction increases drastically.

IV. DISCUSSION

The appearance of cylindrical rolling particles is consistent with experimental observation in silicon/silica [37–40], silicon nitride [41], and rock [43–46] tribosystems. In these experiments, the cylindrical particles are often found to be amorphous [37, 39–41], which is consistent with the amorphous layers found on top of both first and third bodies in our simulation (note that the cores of our wear particles were rigid and therefore impossible to amorphize). In chert (a quartz rock), smooth parts of the surface were found to exhibit cylindrical particles, while rougher parts were free of them [43]. We found that the rollers wear the surface and thus have a polishing effect, which could explain this observation. In the literature, the presence of cylindrical rollers is consistently reported to reduce the friction compared to cases without the rollers [38–40, 45, 46]. Friction coefficients of around $\mu = 0.2$ were observed in silicon/silica systems when rolling particles appeared [38–40], which is similar to our results after running-in. Further comparison with our wear and friction models is not possible, as these works do not report quantitative measurements of the surface roughness.

What can the present results tell us about the life-cycle of the third body and how can it be applied to larger systems? Comparing Eqs. 5 and 6, it is clear that most of the wear volume should be due to wear particle formation. After forming wear particles, though, a relatively low-wear, low-friction regime of roller bearings is entered. The stability of this regime depends on both the proximity of the cylindrical particles, as interaction between them disturbs the rolling motion, and on their size compared to the roughness. If asperities are bigger than the particles, which is plausible in more general situations due to the self-affine scaling of roughness with system size

[54–56], new wear particles are expected to form concurrently and therefore also destabilize the rolling regime. Our results thus seem to suggest that all third bodies in systems comparable to ours invariably tend towards the shear-band-like state and, ultimately, phenomena like cold welding or real shear banding if the third body density is high (ours still is very porous). If the particles are sufficiently far apart and the normal load is not too high, though, it seems that the rolling regime can be maintained over long sliding distances [38–40]. One has also to consider that the friction force will be very high in the shear-band-like regime. This could lead to local heating and melting [45] if heat transport is not efficient enough. If melting can be avoided, the friction force can be reduced by the formation of new, rolling wear particles. This occurs as soon as the local contact size grows to a critical value [12, 57] if the third body has a nonzero shear resistance [14]. In the present work, we can assume that the shear strength of the shear-band-like third body has been reduced to around 4 GPa (as in the bulk amorphous state of the material [14]) or even 3 GPa as suggested by Eq. 3. Then the minimum diameter for newly formed loose wear particles [12, 14] would be approximately 70 nm or 130 nm, respectively, and therefore larger than the simulation cell. We consequently do not observe this formation of new particles.

V. CONCLUSION

We investigated the early stages of the evolution of the third body on the nanoscale, starting with wear particles that increasingly become elongated cylindrical rollers and finally merge to form a porous, shear-band-like layer. We found that the presence of wear particles and surface roughness significantly influences friction and wear at the nanoscale, and simple macroscopic laws are not applicable without modification. This is in contrast to typical sphere-on-flat geometries used in previous work [22]. In the first phase (rolling regime), Amontons–Coulomb friction is enhanced by a term proportional to the surface roughness. A fraction of the frictional work proportional to the surface roughness is used to grow the wear volume. In the second phase (shear-band-like regime), pure Bowden–Tabor-like friction is recovered, which is proportional to the real contact area [47]. This regime exhibits a very low effective wear rate because matter exchange takes place bidirectionally between first and third bodies. Ultimately, third bodies originate from the elementary, nanoscale mechanisms described here. This understanding can provide a pathway to develop physics-based wear models.

ACKNOWLEDGMENT

Financial support by the Swiss National Science Foundation (grant #197152, “Wear across scales”) is gratefully

acknowledged. Computing time was provided by a grant from the Swiss National Supercomputing Centre (CSCS) under project IDs s784 (“The evolution of rough surfaces in the adhesive wear regime”) and s972 (“Surface and subsurface evolution of metals in three-body wear conditions”), as well as by École polytechnique fédérale de Lausanne (EPFL) through the use of the facilities of its Scientific IT and Application Support Center.

AUTHOR CONTRIBUTIONS

T. B. and J.-F. M. designed the study, T. B. ran the simulations and visualized the results, and T. B. and E. M. performed analyses. All authors participated in the preparation of the manuscript.

Appendix A: Choice of material

To simulate the formation of third bodies we needed a material that can sustain a debris layer without welding immediately, while being computationally affordable with regard to time and length scales. We started our search for suitable model materials with a range of realistic metal potentials for Cu [58] and Al [59], as well as a potential [60] suitable for Cu–Ni–Co–Fe high-entropy alloys [61]. Here, we chose two single-crystalline first bodies of size $70 \times 70 \times 58 \text{ nm}^3$ (around 35,000,000 atoms per simulation) with rough surfaces. The abrasive particles quickly scratched the surface, digging into the material. This either lead to a clumping of the particles and suppression of rolling or a quick reduction of the gap between the first bodies and welding. No sustained rolling regime could be observed and friction quickly exceeded 1.0 (Fig. S3 in the Supplemental Material [35]). The suppression of rolling is likely due to a combination of the relatively low hardness of metals with the high adhesion. We therefore also tried to use a Ni–H potential [62], where we manually introduced large amounts of hydrogen into the gap of the nickel–nickel contact at intervals of 1 ns in order to passivate the surfaces. This did not suppress the welding or enable continued rolling of the particles. Since metallic glasses are known for higher hardness than crystalline metals [63], we also performed a test run with a $\text{Cu}_{64}\text{Zr}_{36}$ glass model [64] with first body size of $60 \times 60 \times 29 \text{ nm}^3$ and initially rough surfaces. This system quickly exhibited local surface melting despite the strong thermostats and welded [Fig. S3(g) in the Supplemental Material [35]].

For the main simulations, we therefore chose to use a model potential for a hard, silicon-like material [30, 31], since the above behavior has often been observed for softer systems and metals [12, 17–21]. This potential is a modification of the original Stillinger–Weber potential [30] which reproduces the brittleness of the material [31, 65–67]. While other silicon properties are not reproduced correctly [31], the high hardness and brittleness are optimal to observe wear at the nanoscale at an acceptable com-

putational cost [14]. First bodies of size $58 \times 58 \times 23 \text{ nm}^3$ were created (around 8,000,000 atoms in the simulation cell). Simulations with a single-crystalline model Si in diamond structure showed that sustained rolling of the wear particle could be achieved. Nevertheless, the wear rate was somewhat low (Fig. S5 in the Supplemental Material [35]) and we wanted to avoid the anisotropy of the single crystal. We thus chose a nanocrystalline material created by Voronoi tessellation [68] with average grain size of 2.5 nm. The weak planes introduced by the grain boundaries facilitate a higher wear rate (Fig. S5 in the Supplemental Material [35]) and thus less computational expense to observe the formation of the third body. We therefore used this material for all further investigation.

Appendix B: Choice of initial third body, surface morphology, and simulation size

Our initial investigations of the different materials always used four large wear particles, with diameter 20 nm for the metals and 16 nm for the metallic glass and model silicon. For the nanocrystalline system, we compared a simulation with initially flat surface and round particles to a simulation with initially rough surface and particles in the shape of rhombicuboctahedra. Rough synthetic surface meshes were generated with self-affine roughness [69] using the software TAMAAS [70]. As roughness parameters we used a Hurst exponent of 0.8, a lower wavelength cutoff of 0.5 nm, an upper wavelength cutoff of 11 nm, and an rms of heights of 2 nm. The continuum surface was then used to carve out the atomistic surface. Figure S5(b)–(d) in the Supplemental Material [35] shows that the initial friction force and wear rate of the rough surface were higher in accordance with Eqs. 1 and 6. After running-in, both simulations give equivalent results.

We did not observe particle–particle interactions, though, and decided to reduce the particle size to 8 nm to be able to accommodate 16 particles in the simulation cell. We used mostly rhombicuboctahedra, but verified that the results are comparable with initially round particles (Fig. S6 in the Supplemental Material [35]). For these simulations, we started with the rough surfaces produced by wear with the bigger particles.

In order to speed up the simulations, we also reduced the thickness of the bulk material in z direction from 23 nm to 11 nm for each one of the first bodies. We tested if the thickness influences wear rate or friction force by repeating a sliding simulation with a bulk thickness of 6 nm over a sliding distance of 1 μm . As shown in Fig. S7 in the Supplemental Material [35], we could not detect any difference apart from the expected thermal fluctuations. The atomic shear strain [71] reveals that this is because plastic events occur mostly close to the surface.

Finally, we investigated the initial placement of the wear particles. The rolling regime could be reproduced over a comparatively long sliding distance by having equal spacing between the wear particles, as shown in Fig. 1(b).

This is because adhesive bridges between the particles mostly formed perpendicular to the sliding direction, allowing cylindrical rollers to form. As a comparison, we also placed the particles randomly at the start of the simulation. Due to their close spacing, adhesive bridges in sliding direction occurred and immediately destabilized the rolling regime (Fig. S2 in the Supplemental Material [35]). In reality, a random placement of the particles would always be expected, which means that the rolling cylinders can only remain stable if the interparticle distance remains large during sliding.

Appendix C: Verification simulations

While the sliding velocity is on the order of experimentally achievable velocities, it is nevertheless quite high. We investigated if there are any obvious rate effects by taking a snapshot of the sliding simulation with $F_N = 7.69 \mu\text{N}$ after $s = 1 \mu\text{m}$ and slowing the sliding velocity down to zero over a time of 5 ns. After this, we kept the system static for 5 ns and afterwards ramped up the velocity again over

5 ns. Figure S8 in the Supplemental Material [35] shows that the friction force as a function of sliding distance is not strongly affected by the velocity in this setup. This indicates that the friction force is more sensitive to the surface morphology than to dynamic effects.

The use of rigid particles resembles the abrasive wear case of initially introducing much stiffer and harder wear particles into the system. Here, we end up with a behavior that is closer to abrasive wear due to strong adhesion and the coating of the particles with bulk material. We therefore did short test simulations (for a sliding distance of 10 nm) in which we made the initial wear particles non-rigid and let them deform fully according to the interatomic forces. One of the simulations was restarted from the original run after $s = 1 \mu\text{m}$ (in the rolling regime) and the other after $s = 3 \mu\text{m}$ (in the shear-band-like regime). Figure S9 in the Supplemental Material [35] shows that this does not lead to deviations of the friction force. In the rolling regime, no plasticity was observed inside the originally rigid particles, while the shear-band-like regime exhibited plasticity all over the third body. We therefore expect that the latter will lead to welding more quickly without the rigid particles.

-
- [1] M. Godet, The third-body approach: A mechanical view of wear, *Wear* **100**, 437 (1984).
 - [2] E. E. Brodsky, J. J. Gilchrist, A. Sagy, and C. Collettini, Faults smooth gradually as a function of slip, *Earth Planet. Sci. Lett.* **302**, 185 (2011).
 - [3] K. L. Harris, J. F. Curry, A. A. Pitenis, K. G. Rowe, M. A. Sidebottom, W. G. Sawyer, and B. A. Krick, Wear debris mobility, aligned surface roughness, and the low wear behavior of filled polytetrafluoroethylene, *Tribol. Lett.* **60**, 2 (2015).
 - [4] J. Hintikka, A. Lehtovaara, and A. Mäntylä, Third particle ejection effects on wear with quenched and tempered steel fretting contact, *Tribol. Trans.* **60**, 70 (2017).
 - [5] F.-C. Hsia, F. M. Elam, D. Bonn, B. Weber, and S. E. Franklin, Wear particle dynamics drive the difference between repeated and non-repeated reciprocated sliding, *Tribol. Int.* **142**, 105983 (2020).
 - [6] E. Rabinowicz, *Friction and Wear of Materials*, 2nd ed. (John Wiley & Sons, New York, USA, 1995).
 - [7] T. D. B. Jacobs and A. Martini, Measuring and understanding contact area at the nanoscale: A review, *Appl. Mech. Rev.* **69**, 060802 (2017).
 - [8] C. Q. Yuan, Z. Peng, X. P. Yan, and X. C. Zhou, Surface roughness evolutions in sliding wear process, *Wear* **265**, 341 (2008).
 - [9] F. Deng, G. Tsekenis, and S. M. Rubinstein, Simple law for third-body friction, *Phys. Rev. Lett.* **122**, 135503 (2019).
 - [10] E. Milanese, T. Brink, R. Aghababaei, and J.-F. Molinari, Emergence of self-affine surfaces during adhesive wear, *Nat. Commun.* **10**, 1116 (2019).
 - [11] E. Milanese, T. Brink, R. Aghababaei, and J.-F. Molinari, The role of interfacial adhesion on minimum wear particle size and roughness evolution, *Phys. Rev. E* **102**, 043001 (2020).
 - [12] R. Aghababaei, D. H. Warner, and J.-F. Molinari, Critical length scale controls adhesive wear mechanisms, *Nat. Commun.* **7**, 11816 (2016).
 - [13] R. Aghababaei, D. H. Warner, and J.-F. Molinari, On the debris-level origins of adhesive wear, *Proc. Natl. Acad. Sci. U.S.A.* **114**, 7935 (2017).
 - [14] T. Brink and J.-F. Molinari, Adhesive wear mechanisms in the presence of weak interfaces: Insights from an amorphous model system, *Phys. Rev. Mater.* **3**, 053604 (2019).
 - [15] R. Aghababaei, Effect of adhesion on material removal during adhesive wear, *Phys. Rev. Mater.* **3**, 063604 (2019).
 - [16] E. Milanese and J.-F. Molinari, A mechanistic model for the growth of cylindrical debris particles in the presence of adhesion, *Int. J. Solids Struct.* **203**, 1 (2020).
 - [17] M. R. Sørensen, K. W. Jacobsen, and P. Stoltze, Simulations of atomic-scale sliding friction, *Phys. Rev. B* **53**, 2101 (1996).
 - [18] P. Spijker, G. Anciaux, and J.-F. Molinari, Dry sliding contact between rough surfaces at the atomistic scale, *Tribol. Lett.* **44**, 279 (2011).
 - [19] L. Pastewka, S. Moser, P. Gumbsch, and M. Moseler, Anisotropic mechanical amorphization drives wear in diamond, *Nat. Mater.* **10**, 34 (2011).
 - [20] P. Stoyanov, P. A. Romero, T. T. Järvi, L. Pastewka, M. Scherge, P. Stemmer, A. Fischer, M. Dienwiebel, and M. Moseler, Experimental and numerical atomistic investigation of the third body formation process in dry tungsten/tungsten-carbide tribo couples, *Tribol. Lett.* **50**, 67 (2013).
 - [21] P. A. Romero, T. T. Järvi, N. Beckmann, M. Mrovec, and M. Moseler, Coarse graining and localized plasticity between sliding nanocrystalline metals, *Phys. Rev. Lett.* **113**, 036101 (2014).

- [22] Y. Mo, K. T. Turner, and I. Szułufarska, Friction laws at the nanoscale, *Nature* **457**, 1116 (2009).
- [23] Y. Yang, L. Huang, and Y. Shi, Adhesion suppresses atomic wear in single-asperity sliding, *Wear* **352-353**, 31 (2016).
- [24] T. A. Sharp, L. Pastewka, and M. O. Robbins, Elasticity limits structural superlubricity in large contacts, *Phys. Rev. B* **93**, 121402 (2016).
- [25] T. A. Sharp, L. Pastewka, V. L. Lignères, and M. O. Robbins, Scale- and load-dependent friction in commensurate sphere-on-flat contacts, *Phys. Rev. B* **96**, 155436 (2017).
- [26] S. Eder, G. Feldbauer, D. Bianchi, U. Cihak-Bayr, G. Betz, and A. Vernes, Applicability of macroscopic wear and friction laws on the atomic length scale, *Phys. Rev. Lett.* **115**, 025502 (2015).
- [27] S. Plimpton, Fast parallel algorithms for short-range molecular dynamics, *J. Comp. Phys.* **117**, 1 (1995), <https://lammps.org/>.
- [28] W. M. Brown, P. Wang, S. J. Plimpton, and A. N. Tharrington, Implementing molecular dynamics on hybrid high performance computers – short range forces, *Comput. Phys. Commun.* **182**, 898 (2011).
- [29] W. M. Brown and M. Yamada, Implementing molecular dynamics on hybrid high performance computers—Three-body potentials, *Comput. Phys. Commun.* **184**, 2785 (2013).
- [30] F. H. Stillinger and T. A. Weber, Computer simulation of local order in condensed phases of silicon, *Phys. Rev. B* **31**, 5262 (1985).
- [31] D. Holland and M. Marder, Erratum: Ideal brittle fracture of silicon studied with molecular dynamics [Phys. Rev. Lett. 80, 746 (1998)], *Phys. Rev. Lett.* **81**, 4029 (1998).
- [32] A. Stukowski, Computational analysis methods in atomistic modeling of crystals, *JOM* **66**, 399 (2014).
- [33] A. Stukowski, Visualization and analysis of atomistic simulation data with OVITO – the Open Visualization Tool, *Modell. Simul. Mater. Sci. Eng.* **18**, 015012 (2010), <https://ovito.org/>.
- [34] W. Brostow, M. Chybicki, R. Laskowski, and J. Rybicki, Voronoi polyhedra and Delaunay simplexes in the structural analysis of molecular-dynamics-simulated materials, *Phys. Rev. B* **57**, 13448 (1998).
- [35] See Supplemental Material at the end of this document for figures containing additional data and verification simulations.
- [36] T. Brink, E. Milanese, and J.-F. Molinari, Visualization of simulations for “Effect of wear particles and roughness on nanoscale friction”, Zenodo (2021), <https://doi.org/10.5281/zenodo.4698010>.
- [37] K. Mizuhara and S. M. Hsu, Paper VII (viii) Tribochemical reaction of oxygen and water on silicon surfaces, in *Wear Particles: From the Cradle to the Grave*, Tribology Series, Vol. 21, edited by D. Dowson, C. M. Taylor, T. H. C. Childs, M. Godet, and G. Dalmaz (Elsevier, 1992) pp. 323–328.
- [38] E. Zanoria and S. Danyluk, Ball-on-flat reciprocating sliding wear of single-crystal, semiconductor silicon at room temperature, *Wear* **162-164**, 332 (1993).
- [39] E. Zanoria, S. Danyluk, and M. McNallan, Effects of length, diameter and population density of tribological rolls on friction between self-mated silicon, *Wear* **181-183**, 784 (1995).
- [40] E. S. Zanoria, S. Danyluk, and M. J. McNallan, Formation of cylindrical sliding-wear debris on silicon in humid conditions and elevated temperatures, *Tribol. Trans.* **38**, 721 (1995).
- [41] J. Xu and K. Kato, Formation of tribochemical layer of ceramics sliding in water and its role for low friction, *Wear* **245**, 61 (2000).
- [42] Z. Reches and D. A. Lockner, Fault weakening and earthquake instability by powder lubrication, *Nature* **467**, 452 (2010).
- [43] N. Hayashi and A. Tsutsumi, Deformation textures and mechanical behavior of a hydrated amorphous silica formed along an experimentally produced fault in chert, *Geophys. Res. Lett.* **37**, L12305 (2010).
- [44] Y. Nakamura, J. Muto, H. Nagahama, I. Shimizu, T. Miura, and I. Arakawa, Amorphization of quartz by friction: Implication to silica-gel lubrication of fault surfaces, *Geophys. Res. Lett.* **39**, L21303 (2012).
- [45] X. Chen, A. S. Elwood Madden, and Z. Reches, Friction evolution of granitic faults: Heating controlled transition from powder lubrication to frictional melt, *J. Geophys. Res. Solid Earth* **122**, 9275 (2017).
- [46] X. Chen, A. S. E. Madden, and Z. Reches, Powder rolling as a mechanism of dynamic fault weakening, in *Fault Zone Dynamic Processes: Evolution of Fault Properties During Seismic Rupture*, Geophysical Monograph Series, Vol. 227, edited by M. Y. Thomas, T. M. Mitchell, and H. S. Bhat (American Geophysical Union, 2017) Chap. 7, pp. 133–150.
- [47] F. P. Bowden and D. Tabor, The area of contact between stationary and between moving surfaces, *Proc. R. Soc. Lond. A* **169**, 391 (1939).
- [48] C. A. Coulomb, *Théorie des machines simples en ayant égard au frottement de leurs parties et à la roideur des cordages* (Bachelier, Paris, France, 1821).
- [49] T. Reye, Zur Theorie der Zapfenreibung, *Der Civilingenieur* **6**, 235 (1860).
- [50] E. Rabinowicz and D. Tabor, Metallic transfer between sliding metals: an autoradiographic study, *Proc. R. Soc. Lond. A* **208**, 455 (1951).
- [51] C. A. Queener, T. C. Smith, and W. L. Mitchell, Transient wear of machine parts, *Wear* **8**, 391 (1965).
- [52] J. F. Archard, Contact and rubbing of flat surfaces, *J. Appl. Phys.* **24**, 981 (1953).
- [53] J. F. Archard and W. Hirst, The wear of metals under unlubricated conditions, *Proc. R. Soc. Lond. A* **236**, 397 (1956).
- [54] W. L. Power, T. E. Tullis, and J. D. Weeks, Roughness and wear during brittle faulting, *J. Geophys. Res. Solid Earth* **93**, 15268 (1988).
- [55] B. N. J. Persson, O. Albohr, U. Tartaglino, A. I. Volokitin, and E. Tosatti, On the nature of surface roughness with application to contact mechanics, sealing, rubber friction and adhesion, *J. Phys.: Condens. Matter* **17**, R1 (2005).
- [56] F. Renard, T. Candela, and E. Bouchaud, Constant dimensionality of fault roughness from the scale of microfractures to the scale of continents, *Geophys. Res. Lett.* **40**, 83 (2013).
- [57] T. Brink, L. Frérot, and J.-F. Molinari, A parameter-free mechanistic model of the adhesive wear process of rough surfaces in sliding contact, *J. Mech. Phys. Solids* **147**, 104238 (2021).
- [58] Y. Mishin, M. J. Mehl, D. A. Papaconstantopoulos, A. F. Voter, and J. D. Kress, Structural stability and lattice defects in copper: Ab initio, tight-binding, and embedded-atom calculations, *Phys. Rev. B* **63**, 224106 (2001).

- [59] Y. Mishin, D. Farkas, M. J. Mehl, and D. A. Papaconstantopoulos, Interatomic potentials for monoatomic metals from experimental data and ab initio calculations, *Phys. Rev. B* **59**, 3393 (1999).
- [60] X. W. Zhou, R. A. Johnson, and H. N. G. Wadley, Misfit-energy-increasing dislocations in vapor-deposited CoFe/NiFe multilayers, *Phys. Rev. B* **69**, 144113 (2004).
- [61] L. Koch, F. Granberg, T. Brink, D. Utt, K. Albe, F. Djurabekova, and K. Nordlund, Local segregation versus irradiation effects in high-entropy alloys: Steady-state conditions in a driven system, *J. Appl. Phys.* **122**, 105106 (2017).
- [62] J. E. Angelo, N. R. Moody, and M. I. Baskes, Trapping of hydrogen to lattice defects in nickel, *Modell. Simul. Mater. Sci. Eng.* **3**, 289 (1995).
- [63] C. A. Schuh, T. C. Hufnagel, and U. Ramamurty, Mechanical behavior of amorphous alloys, *Acta Mater.* **55**, 4067 (2007).
- [64] Y. Q. Cheng, E. Ma, and H. W. Sheng, Atomic level structure in multicomponent bulk metallic glass, *Phys. Rev. Lett.* **102**, 245501 (2009), the potential file is the 2011 version from <https://sites.google.com/site/eampotentials/Home/CuZr>.
- [65] D. Holland and M. Marder, Ideal brittle fracture of silicon studied with molecular dynamics, *Phys. Rev. Lett.* **80**, 746 (1998).
- [66] J. A. Hauch, D. Holland, M. P. Marder, and H. L. Swinney, Dynamic fracture in single crystal silicon, *Phys. Rev. Lett.* **82**, 3823 (1999).
- [67] D. Holland and M. Marder, Cracks and atoms, *Adv. Mater.* **11**, 793 (1999).
- [68] P. M. Derlet and H. Van Swygenhoven, Atomic positional disorder in fcc metal nanocrystalline grain boundaries, *Phys. Rev. B* **67**, 014202 (2003).
- [69] J.-J. Wu, Simulation of rough surfaces with FFT, *Tribol. Int.* **33**, 47 (2000).
- [70] L. Frérot, G. Anciaux, V. Rey, S. Pham-Ba, and J.-F. Molinari, Tamaas: a library for elastic-plastic contact of periodic rough surfaces, *J. Open Source Softw.* **5**, 2121 (2020).
- [71] F. Shimizu, S. Ogata, and J. Li, Theory of shear banding in metallic glasses and molecular dynamics calculations, *Mater. Trans.* **48**, 2923 (2007).

Supplemental Material

Effect of wear particles and roughness on nanoscale friction

Tobias Brink, Enrico Milanese, and Jean-François Molinari

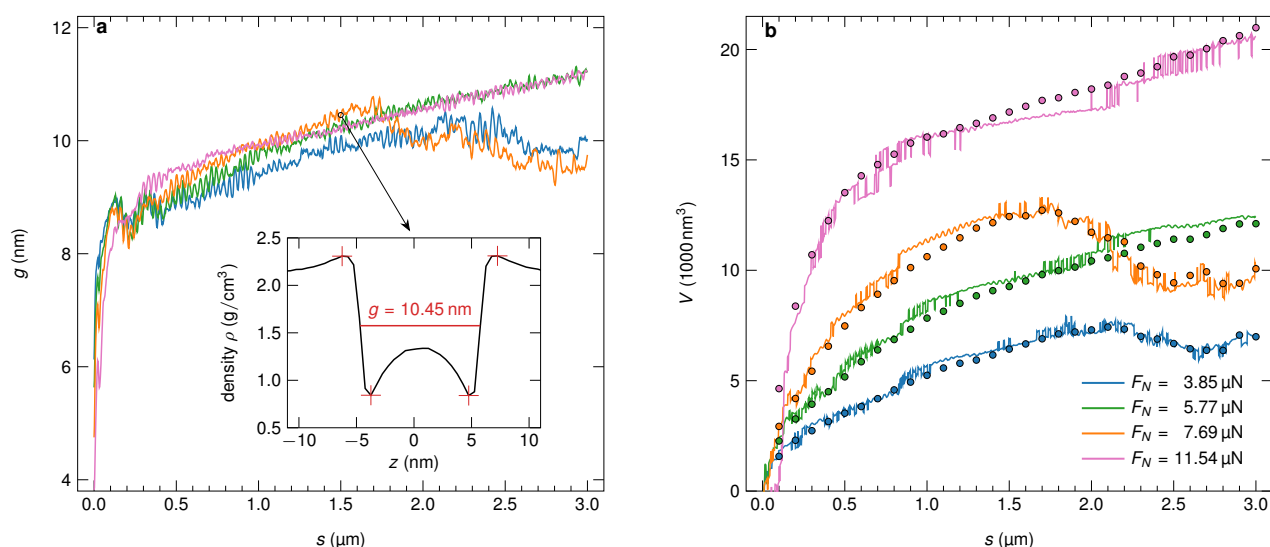


Figure S1: Tribolayer thickness and wear volume calculated from density profiles. **a**, Thickness g of the tribolayer. The continued growth in the rolling regime is in accordance with the agglomeration of mass in the rolling wear particles. It can be seen that the tribolayer width stagnates together with the wear rate in the shear-band-like regime after around $s = 2 \mu\text{m}$ for $F_N = 3.85 \mu\text{N}$ and $7.69 \mu\text{N}$. Inset: Calculation of g from a density profile in z direction (normal to the surfaces). **b**, Wear volume calculated by integrating over the density profile (lines) compared to the computation using the number of atoms in the tribolayer after separation (data points). The lines are shifted to zero at the beginning of the sliding simulation since the integrals include the initial wear particles, which we do not count in the wear volume.

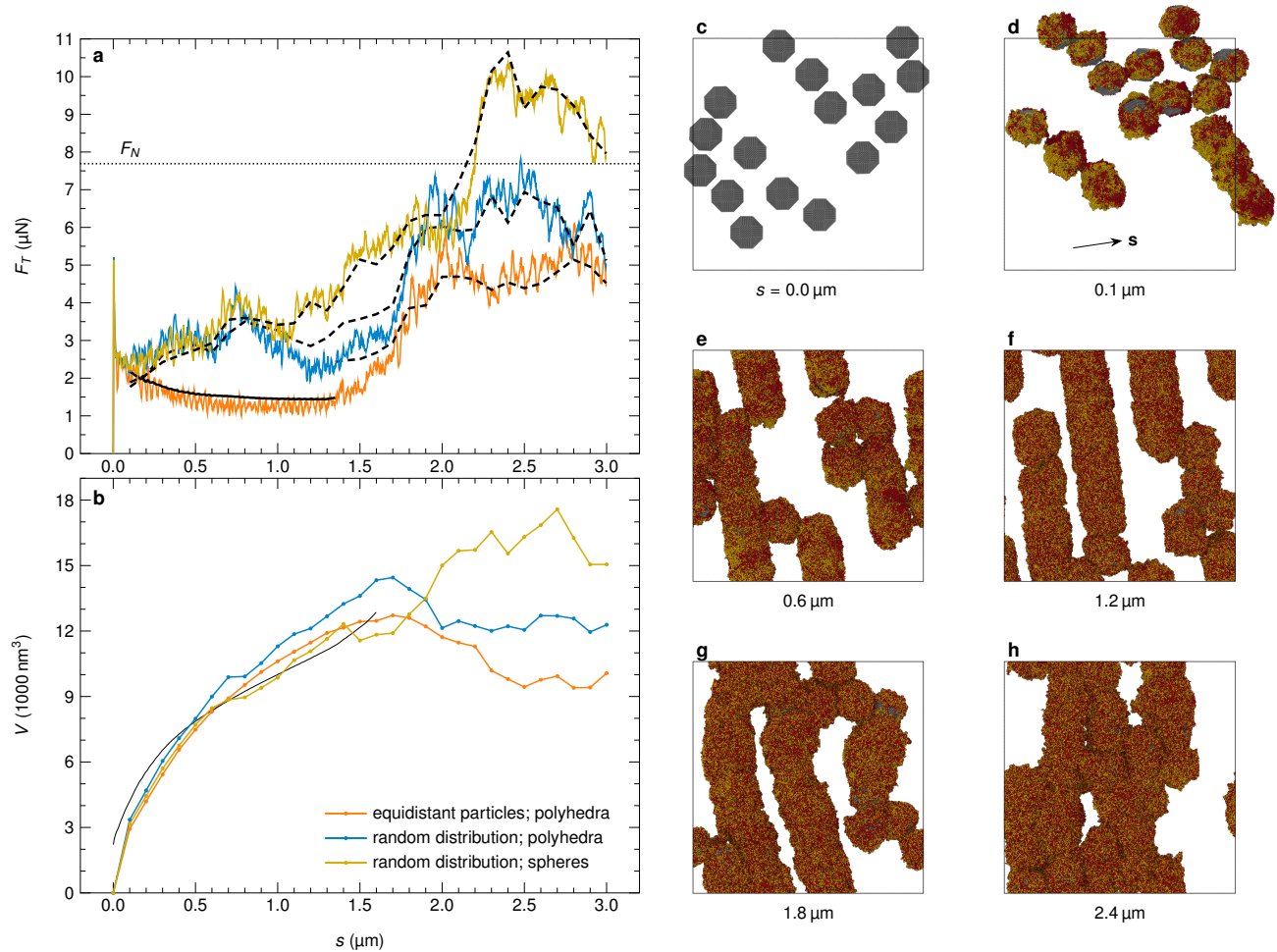


Figure S2: Influence of the initial particle placement. **a**, Compared to the regular arrangement with equidistant particles used for the main results (orange), random initial particle placement leads to an immediate transition to a high-friction regime. Solid black lines correspond to Eq. 1 in the main text, dashed black lines to Eq. 3. **b**, The wear rate does not immediately stagnate, though, as might be expected for the shear-band-like regime. A look at the morphology of the third body (panels **c–h**) can explain this: Parts of the system still clearly consist of rolling cylinders that continue to grow and pick up material. The wear rate only stagnates when all cylindrical particles strongly interact and/or merge (panels **g** and **h**). The solid black line in panel **b** corresponds to Eq. 6 in the main text, computed for the equidistant particles in the rolling regime.

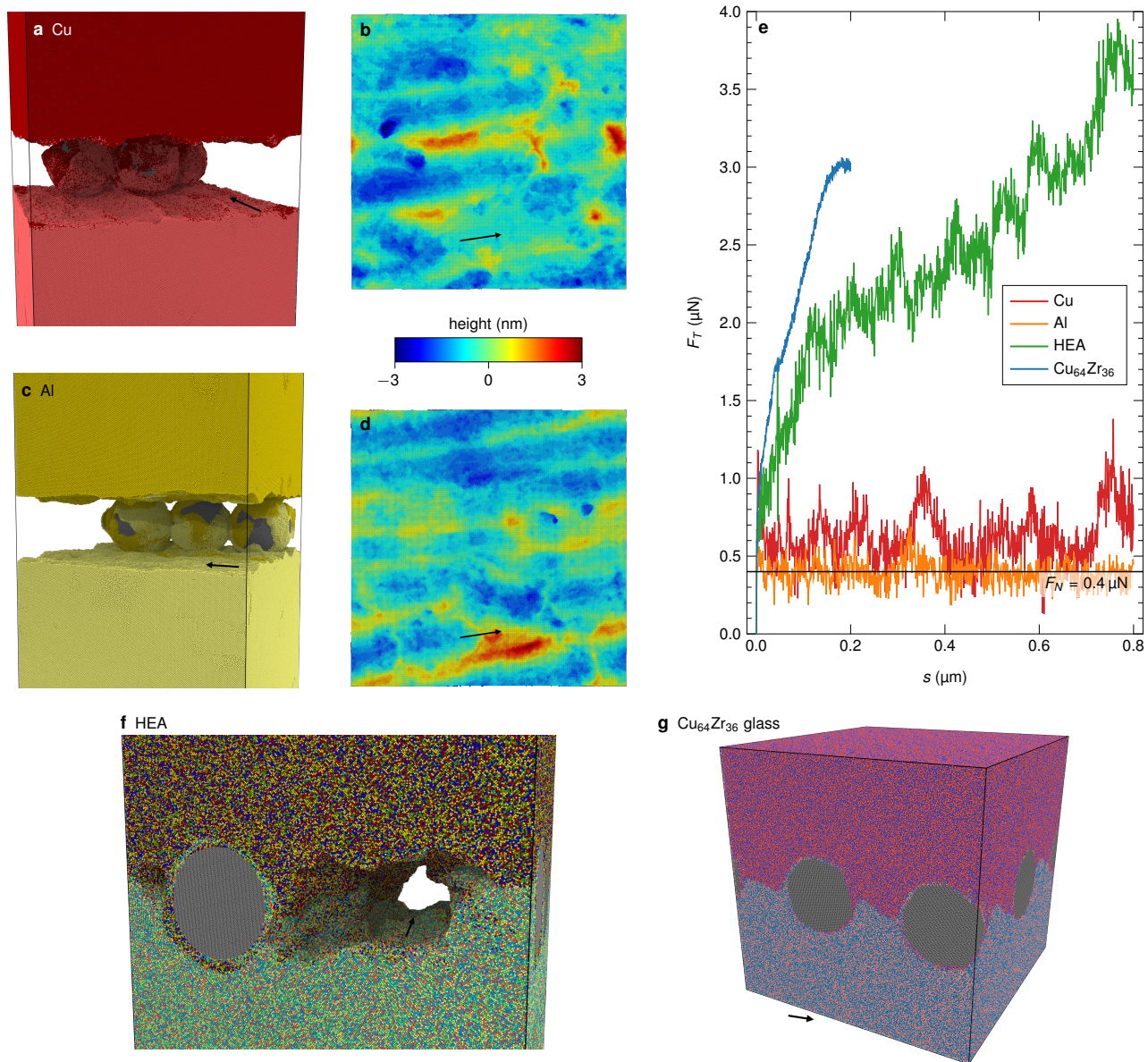


Figure S3: Sliding simulations on different metals. Copper (panels **a** and **b**) and aluminum (panels **c** and **d**) do not exhibit sustained rolling of the wear particles, but the particles stick together almost immediately, leading to scratching (see height maps in panels **b** and **d**) and friction coefficients of one or more (panel **e**). **f**, The high-entropy alloy shows more adhesion and plastic flow than the elemental metals, leading to large pickup of material and very quick welding. **g**, The metallic glass welds instantly due to strong softening of the surface.

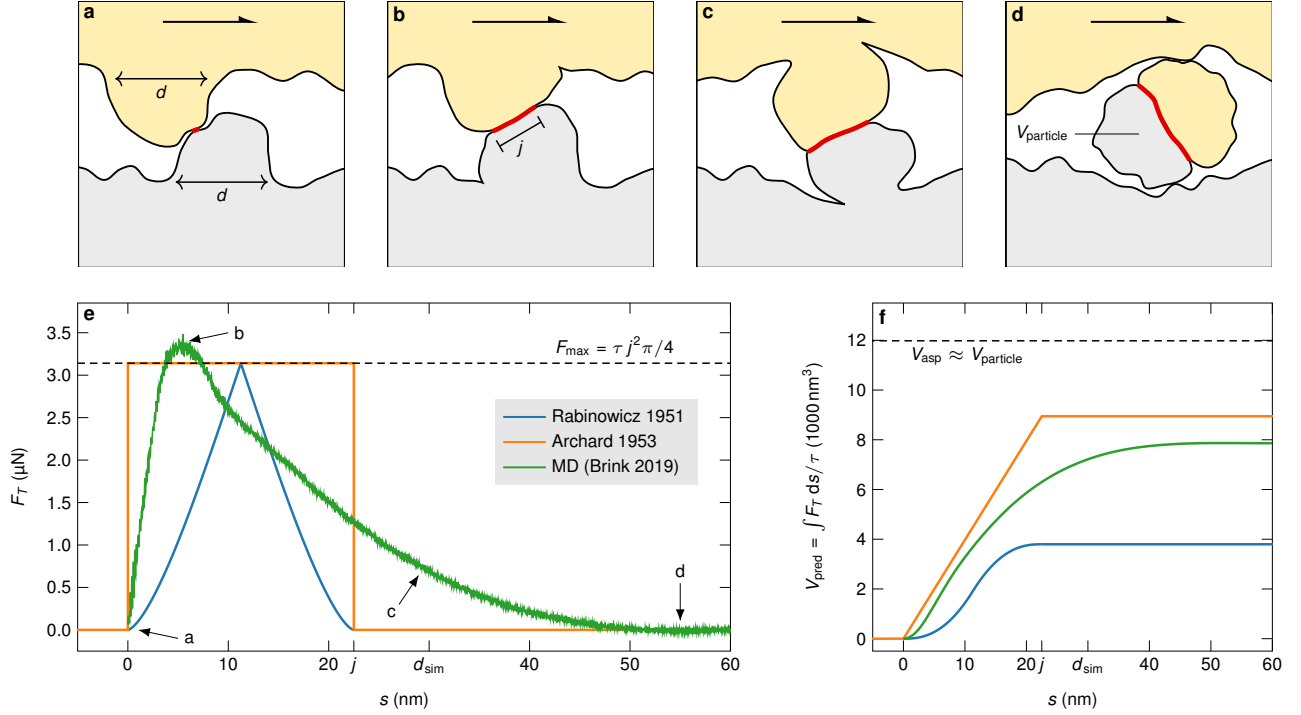


Figure S4: A single-asperity wear law. In the case of wear particle formation with significant plastic activity, it has been found that the wear volume in the single-asperity case is related to the tangential work by [1] $V = \int_0^s F_T ds / \omega \tau \approx F_T s / \omega \tau$ (Eq. 5 in the main text), with ω being a shape factor close to unity. This single-asperity wear law can be derived by assuming that the asperity is loaded to its shear limit τ upon contact (panel a). During sliding, the particle starts to detach (panel b and c) and the full detachment (panel d) will take place at a sliding distance of $s = d$, where d is the asperity diameter, at which point F_T becomes negligible, allowing the approximation of a constant tangential force. The shear limit can be converted to the tangential force via $F_T = \omega \tau d^2$, assuming that the contact area is given by the asperity diameter ($j \approx d$). Measuring only the work $W = \int_0^s F_T ds \approx F_T s$, one can estimate the asperity volume (and therefore the wear particle volume) via $s = d$ and $W / \tau = F_T d / (F_T / \omega d^2) = \omega d^3$. In this simple picture, all dissipation goes into forming a wear particle. In multi-asperity systems, additional frictional dissipation mechanisms occur, wherefore a wear coefficient k is introduced that takes into account that not all the tangential force is used for wear. e, Taking data from an earlier simulation study [2], we can compare the simple models of the tangential force profile by Rabinowicz [3] and Archard [4] with a particle-detachment simulation of a brittle material. As already indicated in panel b, the contact area is given by a contact diameter $j < d$, which we use here instead of d . f, We can also see that the measured wear volume (dashed line) exceeds the predictions, meaning that the wear process is more efficient. The reason is that a brittle asperity is not loaded to its shear limit in all of its volume, since brittle fracture can obviously occur before reaching the elastic limit. Nevertheless, the approximation reproduces the correct order of magnitude [1], as found before.

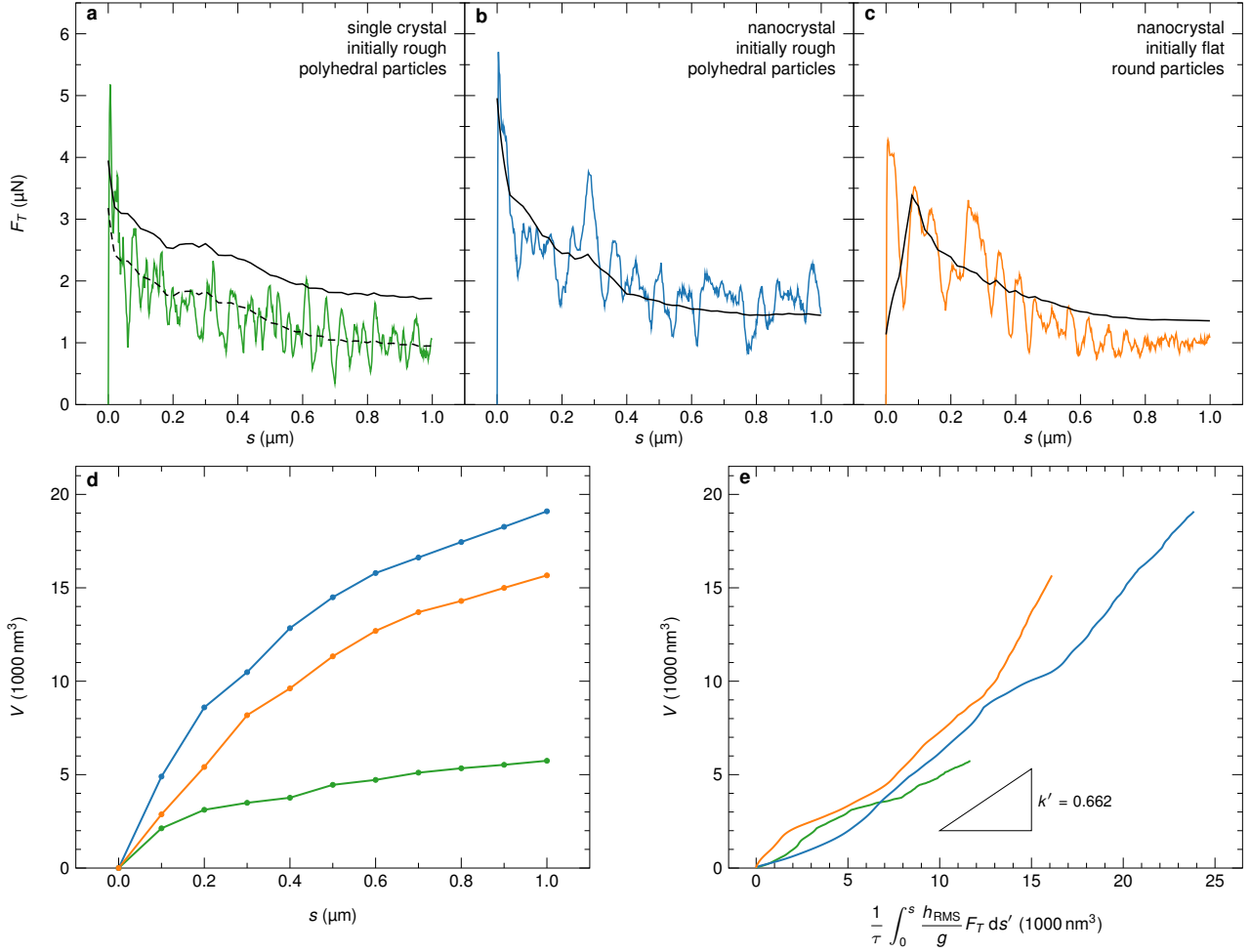


Figure S5: Friction and wear data of the same material used in the main text with four, large initial wear particles. The normal force was $F_N = 7.69 \mu\text{N}$. **a**, For the single-crystalline first bodies, the friction force (green line) is reduced compared to the prediction from the model in Eq. 1 in the main text (solid, black line). A fit (dashed, black line) can be achieved by reducing μ_0^r to 0.03. This indicates that the non-roughness contribution to the friction is lower, possibly due to a reduction of the contact area of the rollers (higher hardness of the single crystal) or due to a reduced effective shear strength (cf. Eq. 2 in the main text). The nanocrystalline first bodies starting from initially rough (panel **b**) and initially flat (panel **c**) surfaces follow the prediction using Eq. 1 in the main text (solid, black lines). **d**, In terms of wear volume, the single-crystalline system wears more slowly and the wear rates of both nanocrystalline systems are similar at the end. As expected, the initial wear rate for the rough surface is higher than for the flat surface. **e**, When plotting the wear volume over the wear prediction from Eq. 6 in the main text (cf. Fig. 4d in the main text), the curves collapse and we obtain approximately the same wear coefficient k' as before.

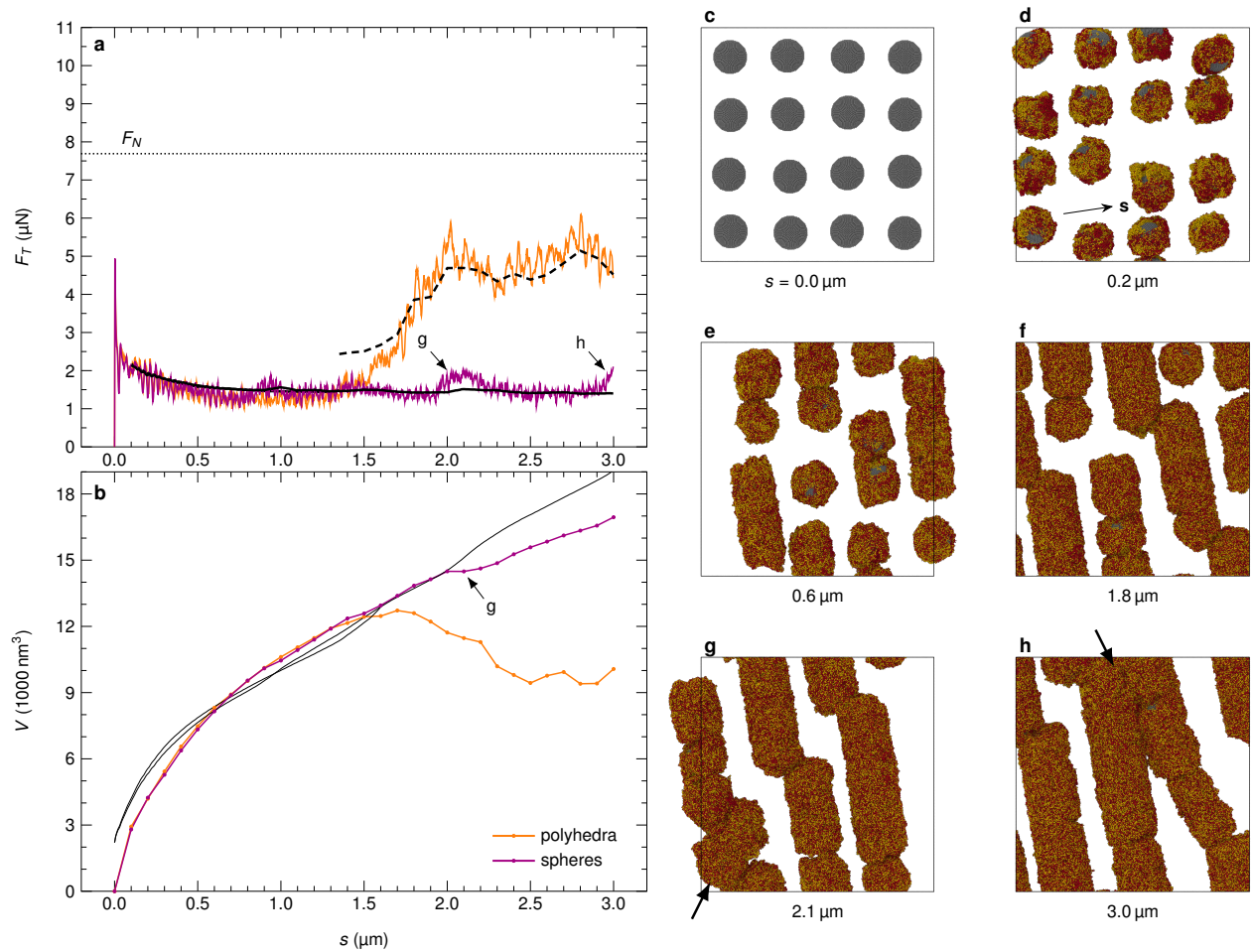


Figure S6: Influence of initial wear particle shape. We tested both polyhedral and round particles, but found that this does not significantly change either the friction (panel **a**) or the wear rate (panel **b**). This is because the particles are quickly coated by material picked up from the first bodies, resulting in the same shape after a short time in both cases. Solid black lines in panel **a** correspond to Eq. 1 in the main text, dashed lines to Eq. 3, and solid black lines in panel **b** correspond to Eq. 6. The only difference between the simulations is when the transition to the shear-band-like regime with high friction and low wear rate occurs. This transition is a stochastic process, though, and thus not a result of the initial particle shape. Panels **c–h** show the evolution of the third body starting from round particles. The rolling regime is retained throughout the simulation. Spikes in the friction can be connected directly to events where the rolling cylinders interact (panels **g** and **h**). Indeed, the transition to the shear-band-like regime seems to initiate already partially at around $s = 2$ μm, where the wear rate becomes lower than the prediction for the rolling regime (panel **b**) and the particles start sticking together (panels **g** and **h**).

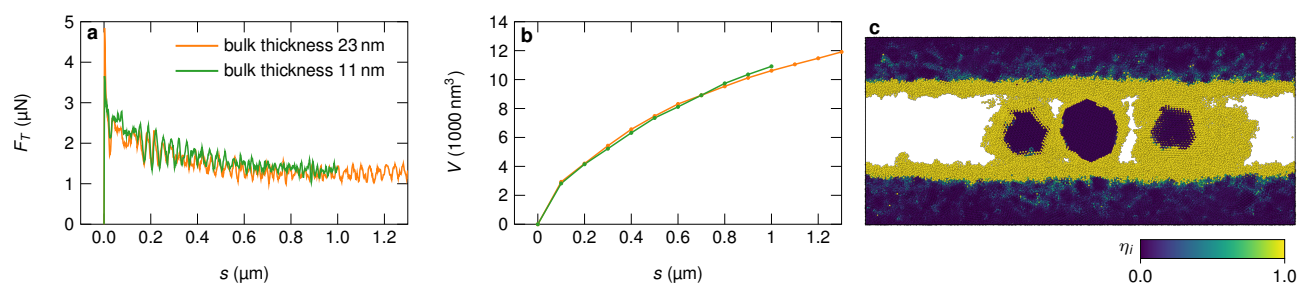


Figure S7: Verification that reducing the initial bulk height does not influence friction or wear within the simulated timescale. Since the system sizes in MD simulations are constrained due to the high computational demands of the method, finite size effects must be excluded. Here, we show that the friction (panel **a**) and wear (panel **b**) response of a system that is much smaller than those in the main results is the same. **c**, This can be explained by the fact that the plasticity, here visualized as the von Mises invariant η_i of the total atomic shear strain [5] at $s = 3 \mu\text{m}$ for the sample with bigger initial bulk thickness, is quite localized at the surface.

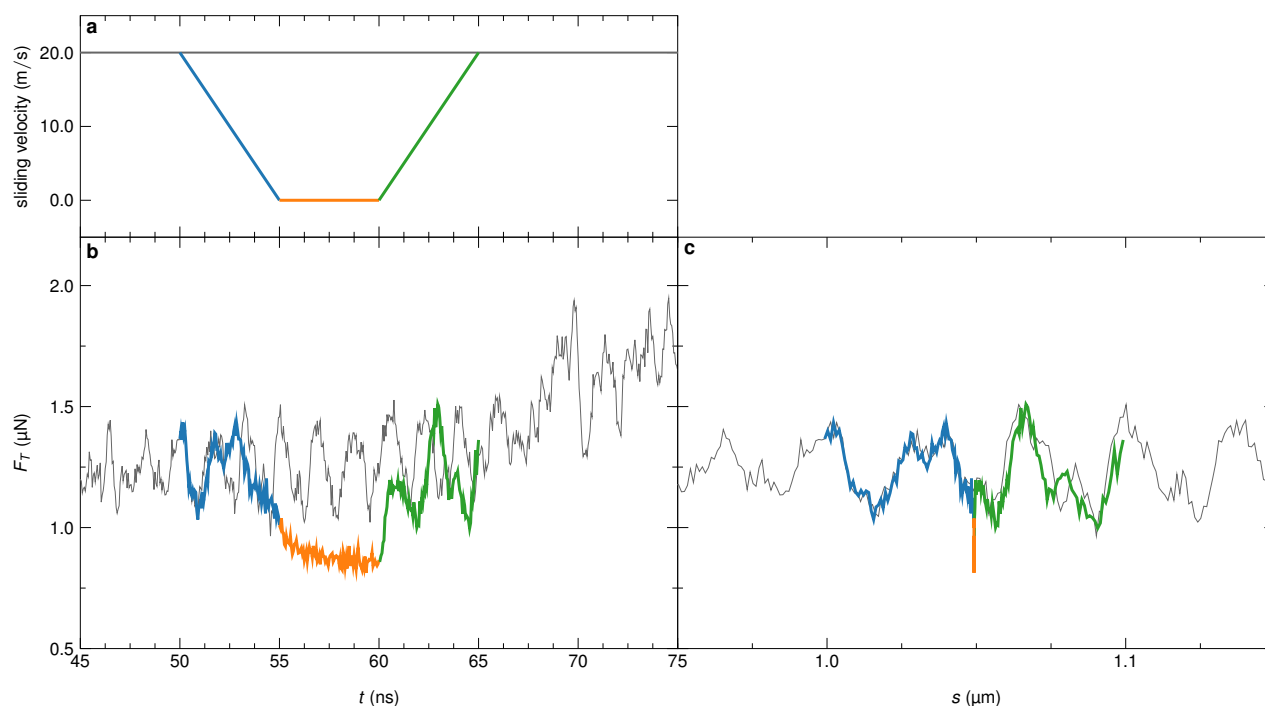


Figure S8: Change of the sliding velocity. **a**, We investigated the influence of the sliding velocity by restarting the sliding simulation with $F_N = 7.69 \mu\text{N}$ at $s = 1 \mu\text{m}$ but then slowly ramping down the velocity from 20 m/s to 0 m/s (blue), holding for 5 ns (orange), and ramping up the velocity again afterwards (green). Grey curves indicate the original, constant velocity simulation. **b**, The friction force relaxes during the holding period, but picks up again quickly afterwards. **c**, When plotting the same data over the sliding distance, it becomes clear that the friction response is not sensitive to the sliding velocity, but to the surface morphology.

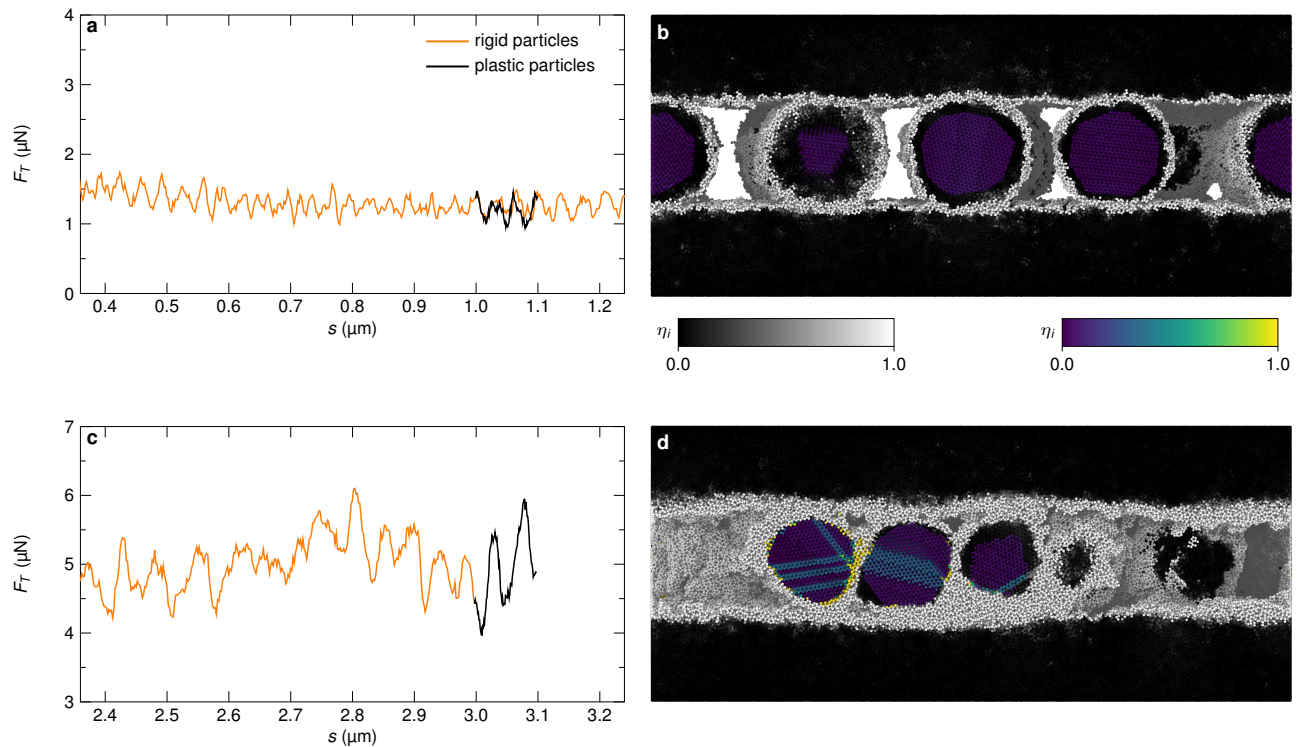


Figure S9: Making the abrasive particles non-rigid. **a**, Restarting the simulation with $F_N = 7.69 \mu\text{N}$ at $s = 1 \mu\text{m}$ in the rolling regime with non-rigid particles does not lead to any change in the friction force response. **b**, The atomic shear strain [5] (blue to yellow: originally rigid particles, black to white: rest of the system) shows no plasticity in the core of the wear particles. **c**, When continuing the simulation at $s = 3 \mu\text{m}$, the friction force is also not affected by the rigidity of the particles. **d**, Nevertheless, plasticity can be observed inside the particles in accordance with the fact that the tribolayer is in a shear-band-like state. Here, shear forces get transmitted through the whole third body.

Supplemental references

- [1] R. Aghababaei, D.H. Warner, and J.-F. Molinari, *On the debris-level origins of adhesive wear*, Proc. Natl. Acad. Sci. U.S.A. **114**, 7935–7940 (2017).
- [2] T. Brink and J.-F. Molinari, *Adhesive wear mechanisms in the presence of weak interfaces: Insights from an amorphous model system*, Phys. Rev. Mater. **3**, 053604 (2019).
- [3] E. Rabinowicz, *The nature of the static and kinetic coefficients of friction*, J. Appl. Phys. **22**, 1373–1379 (1951).
- [4] J.F. Archard, *Contact and rubbing of flat surfaces*, J. Appl. Phys. **24**, 981–988 (1953).
- [5] F. Shimizu, S. Ogata, and J. Li, *Theory of shear banding in metallic glasses and molecular dynamics calculations*, Mater. Trans. **48**, 2923–2927 (2007).